Journal Pre-proof

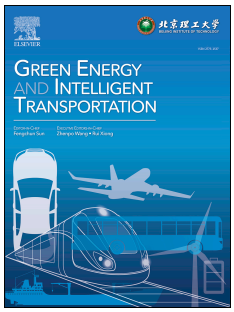

Advancing $LiFePO_4$ battery SOC estimation: Electrochemical impedance spectroscopy with short-period sine-wave pulses

Yizhao Gao, Simona Onori

PII: S2773-1537(25)00136-7

DOI: https://doi.org/10.1016/j.geits.2025.100386

Reference: GEITS 100386

To appear in: *Green Energy and Intelligent Transportation*

Received Date: 30 June 2025

Revised Date: 23 November 2025

Accepted Date: 25 November 2025

Please cite this article as: Gao Y, Onori S, Advancing $LiFePO_4$ battery SOC estimation: Electrochemical impedance spectroscopy with short-period sine-wave pulses, *Green Energy and Intelligent Transportation*, https://doi.org/10.1016/j.geits.2025.100386.

LFP 26650 cell

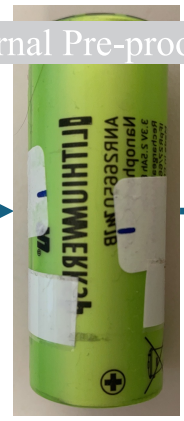

Current

Sine-wave excitation current pulse

α, f

Experimental Voltage response

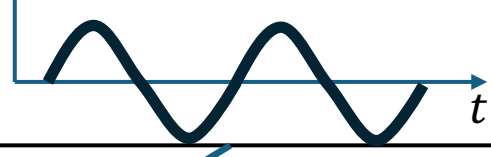

V_t^{exp}

Step 1: Cell impedance identification

$$\widehat{V}_t = V(0) + \alpha|\hat{Z}|\cos\left(2\pi f t + \arg\left(\hat{Z}\right)\right) + [a_0 + \sum_{i=1}^{m} a_i \cos(iwt) + b_i \sin(iwt)]$$

Trigonometric Fourier series

$$\min_{[|\hat{Z}|, \arg(\hat{Z}), a_0, a_i, b_i, w]} \sum_{n=1}^{N} (\hat{V}_{t,n} - V_{t,n}^{exp})^2$$

Recovered impedance $\hat{Z}$ from current/voltage data

$|\hat{Z}|, \arg(\hat{Z})$

Step 2: SOC estimation ($\widehat{SOC}$) based on EIS

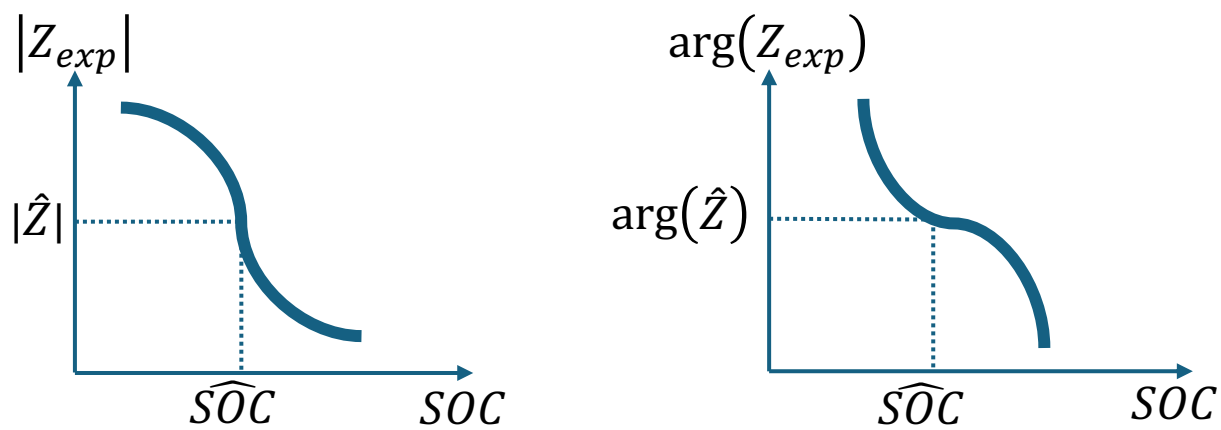

$$\min_{[\widehat{SOC}]} \sqrt{\left(|Z_{exp}(\widehat{SOC})| - |\hat{Z}|\right)^2 + \left(\arg\left(Z_{exp}(\widehat{SOC})\right) - \arg(\hat{Z})\right)^2}$$

Estimated SOC based on EIS

$\widehat{SOC}$

Advancing $LiFePO_4$ Battery SOC Estimation: Electrochemical Impedance Spectroscopy with Short-Period Sine-Wave Pulses

Yizhao Gao*[a], Simona Onori*[a]

[a]Department of Energy Science and Engineering, Stanford University, Stanford, CA 94305, USA

ARTICLE INFO

Keywords:
$LiFePO_4$ batteries
SOC estimation
EIS

ABSTRACT

State-of-charge (SOC) estimation for $LiFePO_4$ (LFP) batteries presents challenges due to their flat open-circuit voltage (OCV). Recent studies suggest that electrochemical impedance spectroscopy (EIS) offers a promising approach for SOC estimation in LFP cells. This work investigates a practical SOC estimation method based on EIS data obtained from short-duration sinusoidal current pulses. First, the EIS of LFP cells is characterized across a broad frequency range [0.01 Hz, 1000 Hz] and SOC range [0, 1]. The EIS magnitude and phase at 0.01 Hz exhibit the highest signal-to-noise ratio (SNR) and are thus selected as features for SOC estimation. An EIS identification algorithm is then developed and validated to reconstruct EIS at 0.01 Hz. This method utilizes Fourier series expansion to approximate the voltage response to small sine-wave current perturbations. SOC estimation is subsequently performed by mapping the reconstructed EIS to experimental EIS data. Finally, the proposed SOC estimation approach is validated using sine-wave currents of varying amplitudes (0.05A and 0.1A) and different cell operation modes (discharge and charge). The results demonstrate rapid and accurate initialization of LFP cell SOC using this estimation algorithm.

1. Introduction

Lithium iron phosphate ($LiFePO_4$, also referred to as LFP) battery technology has gained significant attention as a viable power solution for electric vehicles (EVs), owing to its notable thermal stability and strong resilience to supply-chain [1, 2]. Battery state-of-charge (SOC) estimation is a crucial part of battery management systems (BMSs)[3, 4]. SOC, defined as the ratio of remaining charge to the nominal capacity, is a critical indicator for ensuring safe and efficient battery operation, preventing accelerated degradation [5]. However, direct SOC measurement with sensors is not feasible. Instead, algorithms are needed to estimate SOC from sampled current and voltage signals [6, 7, 8].

Among these algorithms, equivalent-circuit-model (ECM) based Kalman filters, such as the Extended Kalman filter (EKF) [9] and Unscented Kalman filter (UKF) [10], are widely employed for accurate SOC estimation. The relationship between open-circuit voltage (OCV) and SOC is pivotal in battery ECM-based SOC estimation [11], with the OCV slope influencing SOC estimator convergence [12]. Particularly for LFP batteries, the OCV-SOC curve is flat, increasing SOC estimation uncertainty and posing challenges in developing robust SOC estimators [13, 14].

Recently, several techniques have emerged to estimate SOC in LFP batteries, addressing the challenge posed by the flat OCV curve [15]. Electrochemical Impedance Spectroscopy (EIS) is a powerful method for examining battery impedance across various frequencies. This technique involves applying a low-amplitude alternating current (AC) signal to the battery and recording the voltage response. By analyzing the impedance spectra, which depict the battery's frequency-dependent characteristics, valuable insights into internal electrochemical mechanisms such as ion diffusion, charge transfer kinetics, and electrode reactions can be obtained [16]. An EIS-based approach for estimating the SOC of LFP-$Li_4Ti_5O_{12}$ batteries, addressing the challenge of flat open-circuit voltage by leveraging a history-dependent EIS feature was proposed [17]. In this work, a novel in-situ system identification method compatible with standard battery management systems was further developed, enabling real-time EIS extraction using simple current perturbations to accurately infer SOC.

* Corresponding author: Yizhao Gao, yizhaog@stanford.edu; Simona Onori, sonori@stanford.edu.

In Ref. [18], a Nyquist plot was numerically fitted to an RC equivalent circuit, revealing a relationship between SOC and circuit components (e.g., resistance of the double-layer RC and capacitance of the first RC). This approach achieved accurate SOC estimation in the mid-range (20%-80%) with a maximum error of less than 5%. Ref. [19] found that impedance at 1-2 Hz correlates with SOC, while Ref. [20] estimated SOC by identifying variations in equivalent impedance model parameters, derived from impedance measurements at only two frequencies (1.45 Hz and 0.32 Hz). Ref. [21] introduced a fractional-order calculus-based (FOC) model to characterize the constant phase element within the impedance model, using a fractional Kalman filter for SOC estimation. Similarly, Ref. [22] devised an H-infinity observer for SOC estimation, leveraging FOC principles.

The general EIS-based approach involves updating ECM parameters and using these for SOC estimation [23]. Ref.[24] presented a hybrid state-of-health (SOH) estimation framework using EIS-based ECM parameterization and supervised regression, showing that key ECM features, especially ohmic resistance, enable accurate and interpretable SOH prediction across lithium-ion cells. Ref. [25] proposed a novel hybrid SOC estimation approach that integrates EIS data with a combination of data-driven machine learning and equivalent circuit models. Similarly, an alternative strategy employing Deep Neural Networks (DNN) with EIS data was proposed [26]. Ref. [27] observed that the magnitude of EIS at 0.01 Hz changes monotonically with SOC, providing a basis for SOC estimation through impedance measurement at a single frequency (0.01 Hz).

Since a full-frequency EIS scan, especially over low-frequency ranges, can be time-consuming, rapid acquisition of impedance data is essential for enabling the practical integration of EIS-based SOC estimation into BMS. In Ref. [28], a fast method for measuring battery EIS was proposed using the local rational method. This approach, validated through the application of a broadband multi-sine excitation signal lasting 20 seconds over a frequency range of 50 mHz to 100 Hz, demonstrated promising results. In Ref. [29], wavelet transform was applied to process step current and voltage responses, extracting cell impedance at 10 Hz. Additionally, time-domain impedance spectroscopy, based on the Fast Fourier Transform (FFT), was used to measure system impedance simultaneously across all frequencies [30], with an enhanced FFT method facilitating rapid online EIS data acquisition [31].

In Ref. [32], a fast method for battery impedance identification based on pseudo-random binary sequence (PRBS) signals was proposed to accelerate EIS measurements. This approach enables real-time impedance estimation without the need for long rest periods. Similarly, Ref. [33] utilized pulse-like binary multi-frequency signals as excitation signals, significantly reducing test time from 240 seconds to 30 seconds compared to traditional electrochemical workstations. In Ref. [34], a wide-bandwidth EIS identification method was introduced, measuring voltage responses to small-signal current perturbations, which was then used to calibrate an SOC prediction model.

Although EIS remains a widely adopted technique for cell state estimation in lab settings [35], one of the objectives of this work is to leverage readily available current and voltage signals to extract EIS responses, which can then be used to estimate the SOC further. However, most EIS measurements are conducted ex-situ using expensive, specialized instruments. Ref. [36] presented a method to measure battery impedance using excitation current generated by a motor controller, although no SOC estimation algorithm was developed based on the obtained impedance. Ref. [37] proposed an SOC estimation method using multi-sine signal excitations, but the impedance-SOC relationship was not established.

A thorough literature review highlights a gap in the use of sine-wave current profiles for EIS-based SOC estimation. Many studies do not specify the design criteria for selecting frequency points to establish the impedance-SOC relationship, particularly for LFP cells. Additionally, significant challenges remain in using EIS data for SOC estimation. A notable limitation is the absence of dedicated onboard instruments for battery EIS measurement. Furthermore, the relationship between cell impedance and SOC is not well-defined, as impedance depends on both frequency and SOC. While current, voltage, and temperature signals are commonly available in practical BMS, methods for deriving cell impedance from these signals are seldom addressed. Therefore, there is a pressing need for a practical framework that utilizes easily accessible current and voltage data to derive cell impedance, thereby enabling reliable SOC estimation.

The primary objective of this paper is to design short-duration sine-wave current profiles and employ them for SOC estimation in LFP cells based on recovered EIS data. The key contributions of this paper are as follows:

1) Investigation of Signal-to-Noise Ratio (SNR) for EIS-based SOC Estimation: This study thoroughly examines the EIS of LFP cells across a wide frequency range (0.01 Hz to 1000 Hz) and SOC range (0% to 100%). It identifies the EIS at 0.01 Hz as having the highest SNR, making it a key feature for SOC estimation. This insight is critical for improving the accuracy of SOC estimation, particularly in addressing the flat OCV-SOC curve challenge in LFP batteries.
2) Introduction of a Rapid EIS Recovery Strategy Using Short-Duration Sinusoidal Pulses: The paper presents a novel method for recovering the EIS data of LFP cells using short-duration sinusoidal current pulses. By employing Fourier series expansion, the method approximates the voltage response, significantly reducing the time required for EIS measurements. This approach allows for efficient SOC estimation without the need for expensive, specialized equipment, making it more practical for integration into real-world BMSs.
3) Development of an EIS-Based SOC Estimation Algorithm: The study develops and validates an algorithm that uses recovered EIS data to estimate the SOC of LFP cells. By mapping the reconstructed EIS to experimental data, the algorithm mitigates the uncertainties caused by the flat OCV-SOC relationship in LFP cells. The proposed method is tested with varying sine-wave current amplitudes (0.05A and 0.1A) and demonstrates robust SOC estimation during both charge and discharge cycles.

2. Cell Experimental Design

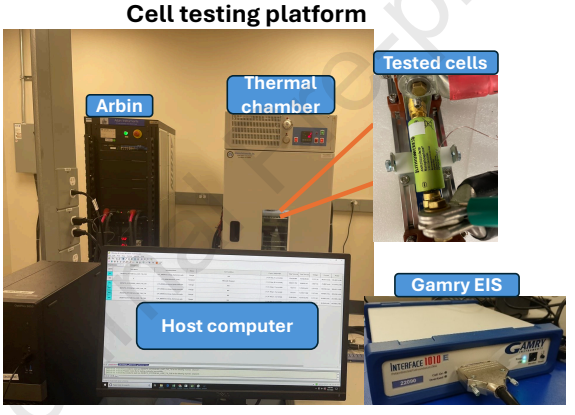

Figure 1: Cell testing platform at Stanford Energy Control Lab [38].

Table 1
26650 cylindrical LFP cell specification

Nominal capacity	2.5 Ah
Nominal voltage	3.3 V
Cathode chemistry	$LiFePO_4$
Anode chemistry	Graphite

In this section, the experimental setup of the cell testing platform including the cell EIS and sine-wave current pulse testing is introduced.

This study examines the commercial 26650 cylindrical LFP cells, with specifications detailed in Table 1 . The cells are placed in the AMEREX IC500R thermal chamber and are cycled using the Arbin LBT21024. Cycling of the cells (discharge/charge) is conducted using an Arbin tester, while cell EIS measurements are performed with Gamry interfaced with the Arbin battery testing system, as shown in Fig. 1. All experiments in this paper were conducted under controlled isothermal conditions at 25°C.

Two tests were conducted: the EIS test and the sine-wave pulse current test. For the EIS test in the discharge direction (Fig. 2), the cell is first fully charged using the constant current-constant voltage (CC-CV) method (Step 1), followed by a 2-hour rest (Step 2). A rest period of 2 hours was chosen to ensure

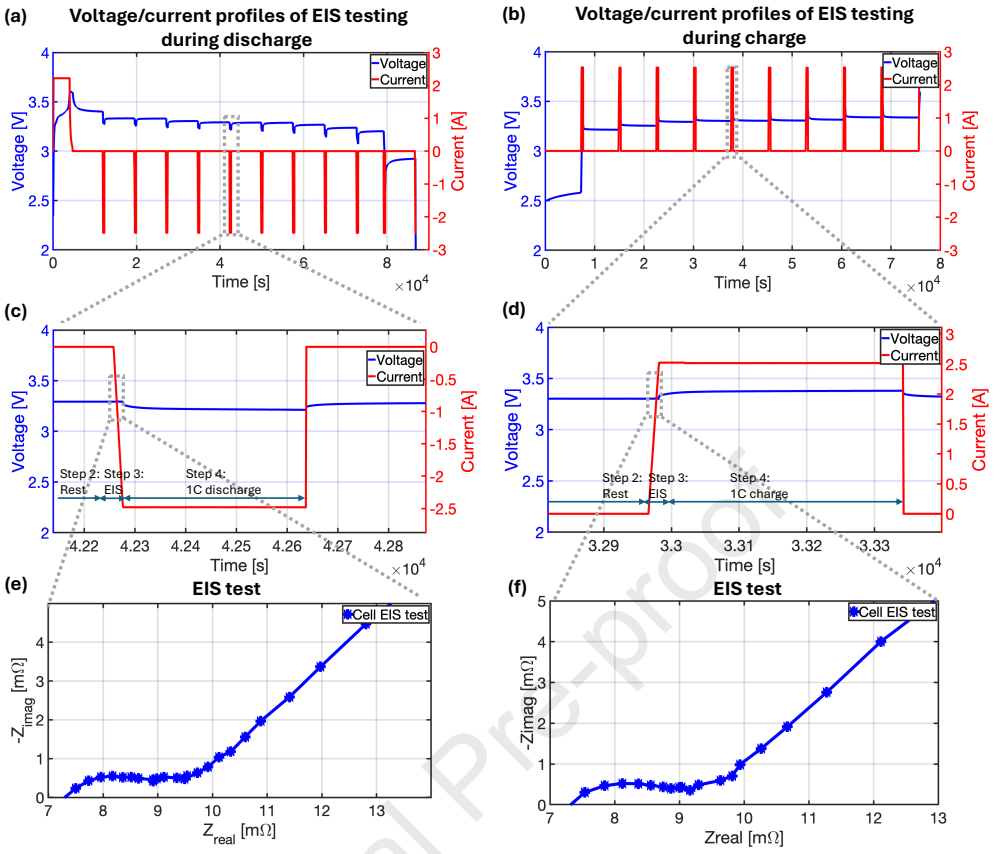

Figure 2: Voltage and current profiles of EIS testing under different operating directions. (a) Cell voltage and current profiles during discharge. (b) Cell voltage and current profiles during charge. (c) Zoomed-in view of Steps 2–4 at 60% SOC during discharge. (d) Zoomed-in view of Steps 2–4 at 40% SOC during charge. (e) One EIS result at 60% SOC during discharge. (f) One EIS result at 40% SOC during charge.

that the cell reached a fully relaxed state prior to EIS or sine-wave excitation. This duration allowed the electrochemical system to return to equilibrium after previous cycling, thereby minimizing the influence of transient diffusion or relaxation processes on the impedance response. The EIS test (Step 3) was conducted in galvanostatic mode. Galvanostatic EIS measurements were carried out using a frequency-sweep protocol from 1000 Hz down to 0.01 Hz, with an AC current amplitude of 0.1 A or 0.05 A. After each EIS test, the cell is discharged by 10% SOC (Step 4), repeating steps 1–4 until the lower cut-off voltage is reached (fully discharged).

For the EIS measurements in the charge direction, the cell is initially brought to the fully discharged state (Step 1). The testing protocol is similar to that for the discharge direction: the cell is charged in 10% SOC increments (Step 4), and steps 1–4 are repeated at each increment until the upper cut-off voltage is reached. The voltage and current profiles for both directions are shown in Fig. 2a and Fig. 2b, while the results of the EIS test of a single cycle are presented in Fig. 2e and Fig. 2f.

For the sine-wave pulse current test (Fig. 3), steps 1, 2, and 4 are identical to those of the EIS test, but in Step 3, a sine-wave pulse current excitation is applied instead of EIS testing. Two current profiles with amplitudes of 0.1 A or 0.05 A were applied, each at a frequency of 0.01 Hz. Voltage and current profiles during testing are shown in Fig. 3a and Fig. 3b, and the sine-wave current and voltage profiles from a single cycle are depicted in Fig. 3e and Fig. 3f. In the experimental design, current amplitudes of 0.05 A and 0.1 A were selected as they represent typical small-signal excitation levels for 2.5 Ah LFP cells. These magnitudes are sufficiently low to preserve electrochemical linearity while still maintaining an adequate signal-to-noise

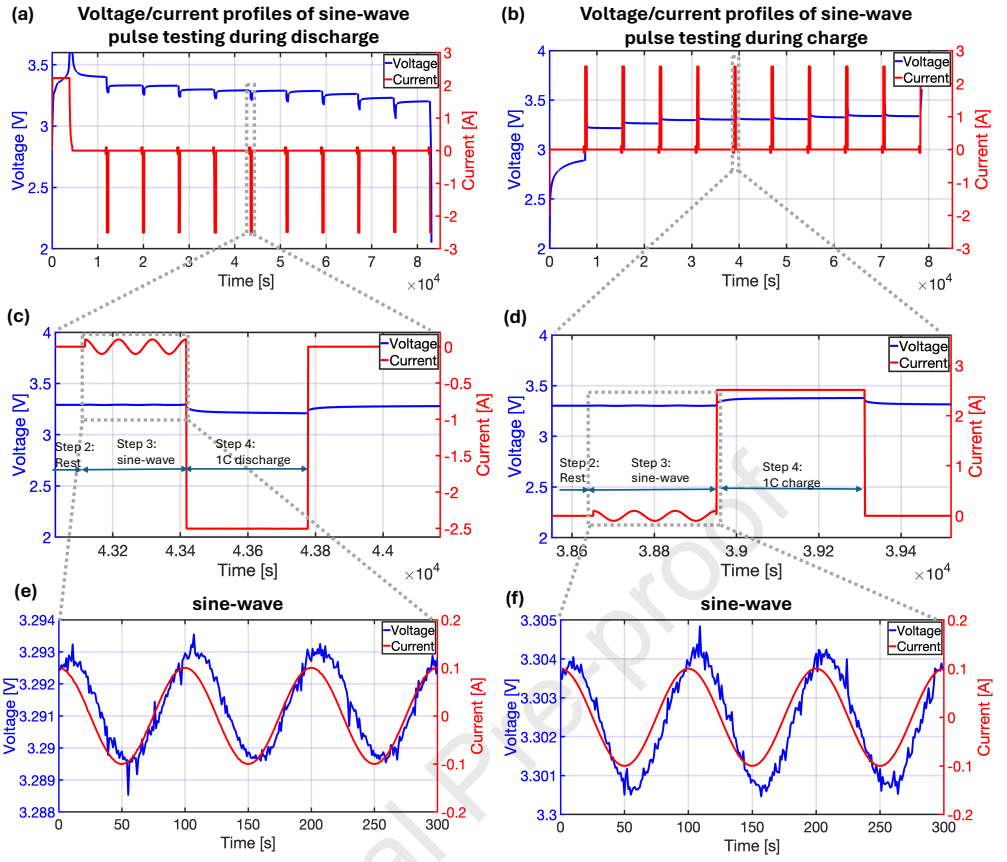

Figure 3: Voltage and current profiles of sine-wave pulse testing under different operating directions. (a) Cell voltage and current profiles during discharge. (b) Cell voltage and current profiles during charge. (c) Zoomed-in view of Steps 2–4 at 60% SOC during discharge. (d) Zoomed-in view of Steps 2–4 at 40% SOC during charge. (e) One sine-wave pulse at 60% SOC during discharge. (f) One sine-wave pulse at 40% SOC during charge.

ratio for reliable impedance identification. This balance ensures that the measurements reflect intrinsic cell dynamics without introducing nonlinear distortions.

All experimental procedures, data acquisition protocols, and dataset structures are detailed in the supplementary information. To maintain conciseness, these details are not repeated in the main text. Readers may refer to the supplementary information for full reproducibility.

3. Methodology

In this section, the EIS testing results with protocols introduced in section 2 are analyzed. The SNR of EIS magnitudes and phases at different frequencies are calculated and compared. The SOC estimation algorithm based on the EIS recovery strategy with sine-wave current pulse excitation is introduced.

3.1. EIS versus SOC analysis

Fig. 4a-d present EIS testing results under galvanostatic mode at two current amplitudes of 0.1A and 0.05A across 10 SOC points, spaced in increments of 0.1, during both discharge and charge. In Fig. 4a, EIS predominantly consists of arcs representing high-frequency charge transfer processes and straight lines representing low-frequency diffusion processes. At higher SOC, the semicircle arcs exhibit a smaller curvature radius, indicating reduced lithium intercalation resistance in the lithium iron phosphate electrode and more facile charge-transfer kinetics. Notably, in the low-frequency region indicative of diffusion, the behavior of the battery's diffusion lines undergoes a noticeable change with SOC. Specifically, higher SOC values result in lower impedance. At 0.01 Hz, SOC exerts the greatest impact on EIS, prompting

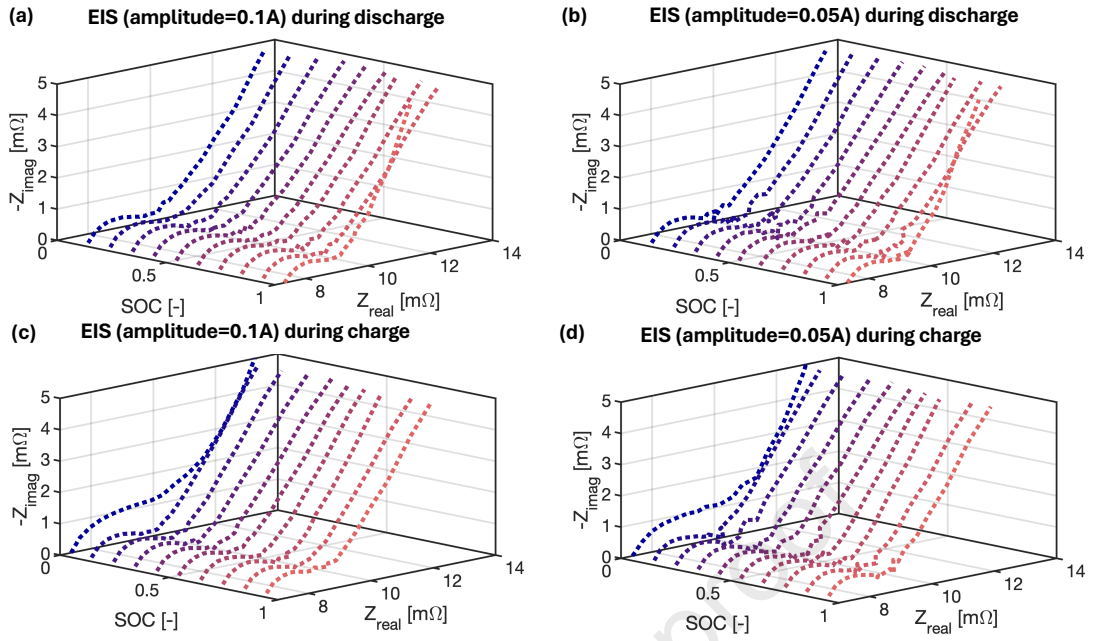

Figure 4: (a) Cell EIS results obtained in galvanostatic mode (amplitude = 0.1 A) at various SOC levels during discharge. (b) Cell EIS results obtained in galvanostatic mode (amplitude = 0.05 A) at various SOC levels during discharge. (c) Cell EIS results obtained in galvanostatic mode (amplitude = 0.1 A) at various SOC levels during charge. (d) Cell EIS results obtained in galvanostatic mode (amplitude = 0.05 A) at various SOC levels during charge.

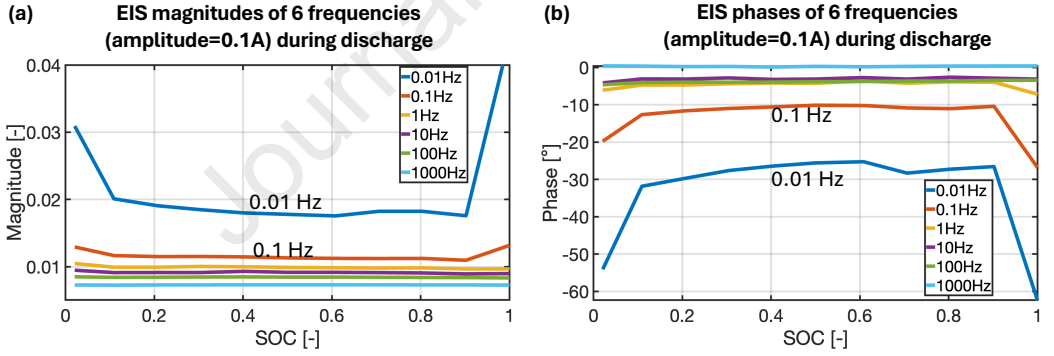

Figure 5: (a) LFP cell EIS magnitudes of 6 different frequencies (0.01 Hz, 0.1 Hz, 1 Hz, 10 Hz, 100 Hz, 1000 Hz), (galvanostatic mode, amplitude=0.1A) under different SOC points during discharge. (b) LFP cell EIS phases of 6 different frequencies (0.01 Hz, 0.1 Hz, 1 Hz, 10 Hz, 100 Hz, 1000 Hz), (galvanostatic mode, amplitude=0.1A) under different SOC points during discharge.

consideration of an EIS-based SOC estimation strategy. Similar EIS behavior is observed in Fig. 4c, where differentiation between EIS curves is more apparent in the low-frequency range compared to the high-frequency range. When the excitation amplitude decreases to 0.05 A, subtle increases in measurement variability can be observed, especially in the mid-frequency region. Due to the lower current, the signal intensity is relatively weaker, resulting in a more significant impact of noise on the measurement. However, it is still evident from Fig. 4b and Fig. 4d that the EIS curves are sensitive to SOC variation in the low-frequency range. Next, we will demonstrate the suitability of the EIS at 0.01 Hz as the optimal feature for EIS-based SOC estimation among various frequencies.

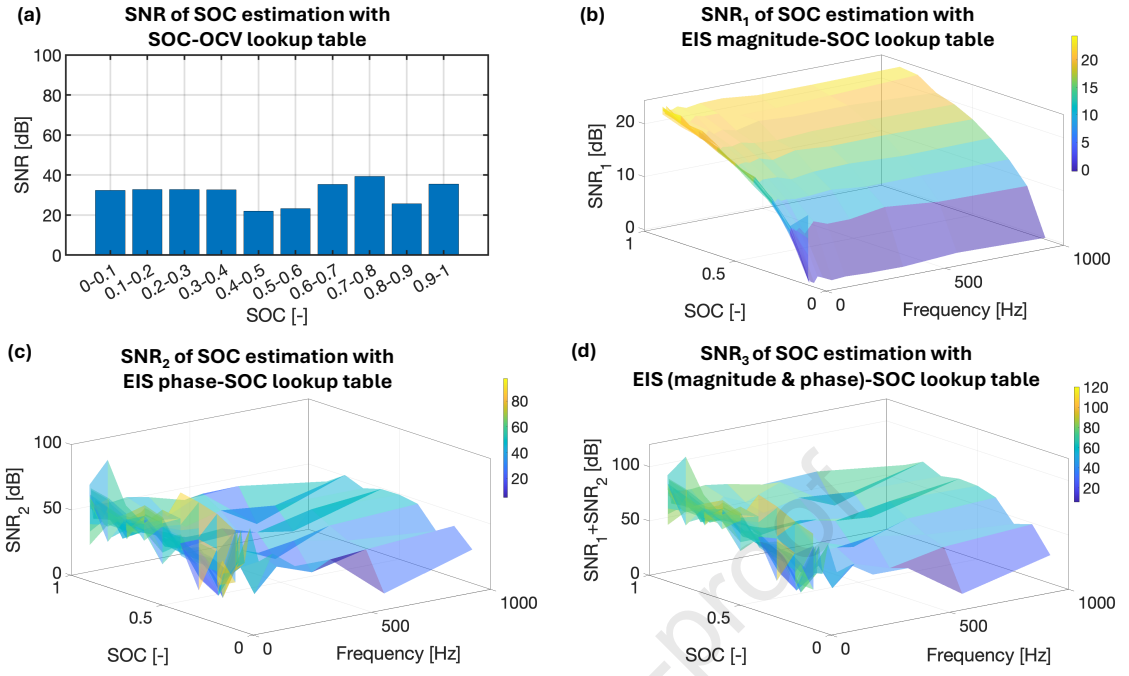

Figure 6: (a) SNR of SOC estimation only with SOC-OCV lookup table after White Gaussian noise is added to the OCV (SNR= 55 dB) at different SOC ranges. (b) SNR of SOC estimation only with SOC-EIS magnitude lookup table after White Gaussian noise is added to the EIS magnitude at different SOC ranges. (c) SNR of SOC estimation only with SOC-EIS phase lookup table after White Gaussian noise is added to the EIS phase (SNR= 55 dB) at different SOC ranges. (d) SNR of SOC estimation with SOC-EIS phase & magnitude lookup table after White Gaussian noise is added to the EIS magnitude and phase (SNR= 55 dB) at different SOC ranges.

Fig. 5 presents a summary of the EIS magnitudes and phases across 6 frequencies (0.01 Hz, 0.1 Hz, 1 Hz, 10 Hz, 100 Hz, 1000 Hz) for the case of 0.1 A amplitude. In Fig. 5a, the EIS magnitudes show minimal variation with SOC in the mid- to high-frequency range (1-1000 Hz). In contrast, the low-frequency region (0.01-0.1 Hz) exhibits a much stronger SOC dependence, with the steepest slope occurring at 0.01 Hz. A similar pattern is observed in Fig. 5b, where the SOC-induced variation in phase is also greatest at 0.01 Hz relative to the other frequencies. Notably, considering the flatness of the LFP OCV versus SOC, SOC estimation becomes increasingly challenging. Given the substantial slope exhibited by the EIS versus SOC at 0.01 Hz compared to other frequencies, it suggests a high dependency of cell impedance on SOC at this specific frequency. This observation underscores the rationale for pursuing EIS-based SOC estimation anchored on the EIS feature at 0.01 Hz.

The SNR serves as a valuable metric for assessing the relative strength of a desired signal in comparison to background noise. It is quantified as the ratio of signal power to noise power, commonly denoted in decibels. Typically, a higher SNR indicates a lesser degree of noise interference within the signal, signifying superior signal fidelity. Therefore, a high SNR value is advantageous for accurate state estimation. In this context, we employ SNR as a measure of the robustness of SOC estimation. Initially, we examine the SNR pertaining to SOC estimation, leveraging solely the OCV-SOC lookup table. By adding a small White Gaussian noise (SNR=55 dB) to the OCV ($\widehat{OCV}$), the SNR of the SOC estimation with OCV-SOC lookup ($SNR_{\widehat{SOC}_{OCV-SOC:look-up-table}}$) table is defined as:

$$\widehat{SOC}_{OCV-SOC:look-up-table} = f_{OCV-SOC}(\widehat{OCV}) \tag{1}$$

$$\mathrm{SNR}_{\widehat{\mathrm{SOC}}_{\text{OCV-SOC:look-up-table}}} = 20\log_{10}\left(\frac{\sqrt{\sum_{n=1}^{N}\left|\widehat{\mathrm{SOC}}_{\text{OCV-SOC:look-up-table},n}\right|^2}}{\sqrt{\sum_{n=1}^{N}\left|\text{noise}_n\right|^2}}\right) \tag{2}$$

where $f_{OCV-SOC}(\widehat{OCV})$ is the lookup table function representing the SOC corresponding to a given OCV value ($\widehat{OCV}$). N is the length of $\widehat{SOC}_{OCV-SOC:look-up-table}$ vector estimated only with the OCV-SOC look-up table method. $\widehat{\mathrm{SOC}}_{\text{OCV-SOC:look-up-table},n}$ is the n-th component. noise$_n$ is the n-th component of the noise vector.

Similarly, the SNRs of the SOC estimation with EIS magnitude $\left|\hat{Z}\right|$-SOC (SNR_1=$SNR_{\widehat{SOC}_{|\hat{Z}|-SOC:look-up-table}}$), EIS phase $arg\hat{Z}$-SOC (SNR_2=$SNR_{\widehat{SOC}_{arg\hat{Z}-SOC:look-up-table}}$), and EIS (magnitude & phase)-SOC lookup table(SNR_3=$SNR_{\widehat{SOC}_{|\hat{Z}|\&arg\hat{Z}-SOC:look-up-table}}$) are calculated by replacing the OCV in Eqs.1-2 with $\left|\hat{Z}\right|$, $arg\hat{Z}$, and $\left|\hat{Z}\right|$ &$arg\hat{Z}$, respectively. The calculation equations of SNR_1, SNR_2, and SNR_3 are listed in the Appendix.

The SNR analysis of SOC estimation methods for the LFP cell considered in this work using OCV-SOC and EIS lookup tables is shown in Fig. 6. In Fig. 6a, the OCV-SOC lookup table results in a reduced SNR (less than 40 dB) under small OCV noise. Similarly, Fig. 6b shows that using only the EIS magnitude-SOC lookup table also yields a low SNR (less than 40 dB) under slight OCV noise. These findings suggest that integrating the EIS phase-SOC relationship could in principle improve the accuracy of LFP SOC estimation compared to solely relying on the OCV-SOC relationship. Notably, the EIS phase-SOC lookup table significantly increases SNR, as seen in Fig. 6c. Furthermore, combining the EIS magnitude and phase-SOC lookup tables (Fig. 6d) results in higher SNRs than using either the magnitude or phase-SOC table alone. This combined approach achieves the highest SNR at 0.01 Hz across the frequency spectrum (0.01 Hz to 1000 Hz). Based on these results, we identify the EIS-SOC relationship at 0.01 Hz as the most promising feature for SOC estimation.

3.2. EIS-based SOC framework

The high SNR values observed in the EIS versus SOC at 0.01Hz suggest a potential enhancement in the robustness of SOC estimation compared to methods relying solely on OCV-SOC correlations. The finding is particularly promising for EIS-based SOC estimation. We proceed to develop an algorithm for EIS-based SOC estimation. The framework for EIS-based SOC estimation is illustrated in Fig. 7. The framework consists of two key steps. The first step identifies the cell's EIS using a sinusoidal excitation signal. The second step estimates the cell's SOC based on the recovered EIS information.

Recognizing the challenges associated with measuring direct frequency-domain EIS signals in real-time, we derive the EIS signal from time-domain current and voltage data. The cell impedance, represented as $Z(j2\pi f)$, comprises both magnitude and phase components:

$$Z(j2\pi f) = -|Z(j2\pi f)|\, e^{j\ \arg(Z(j2\pi f))} \tag{3}$$

where $|Z(j2\pi f)|$ is the magnitude of the cell impedance and $\arg(Z(j2\pi f))$ is the phase of the impedance. Ideally, for EIS testing in galvanostatic mode, a sinusoidal current $i(t)$ is applied to the cell around the cell OCV :

$$i(t) = \alpha cos(2\pi f t) \tag{4}$$

where α is the amplitude (A), f is the frequency (Hz), and t is time (s).

The voltage response from the excitation current can be measured as:

$$\hat{V}_t = V_t(0) + \alpha|Z|\cos(2\pi f t + \arg(Z)) \tag{5}$$

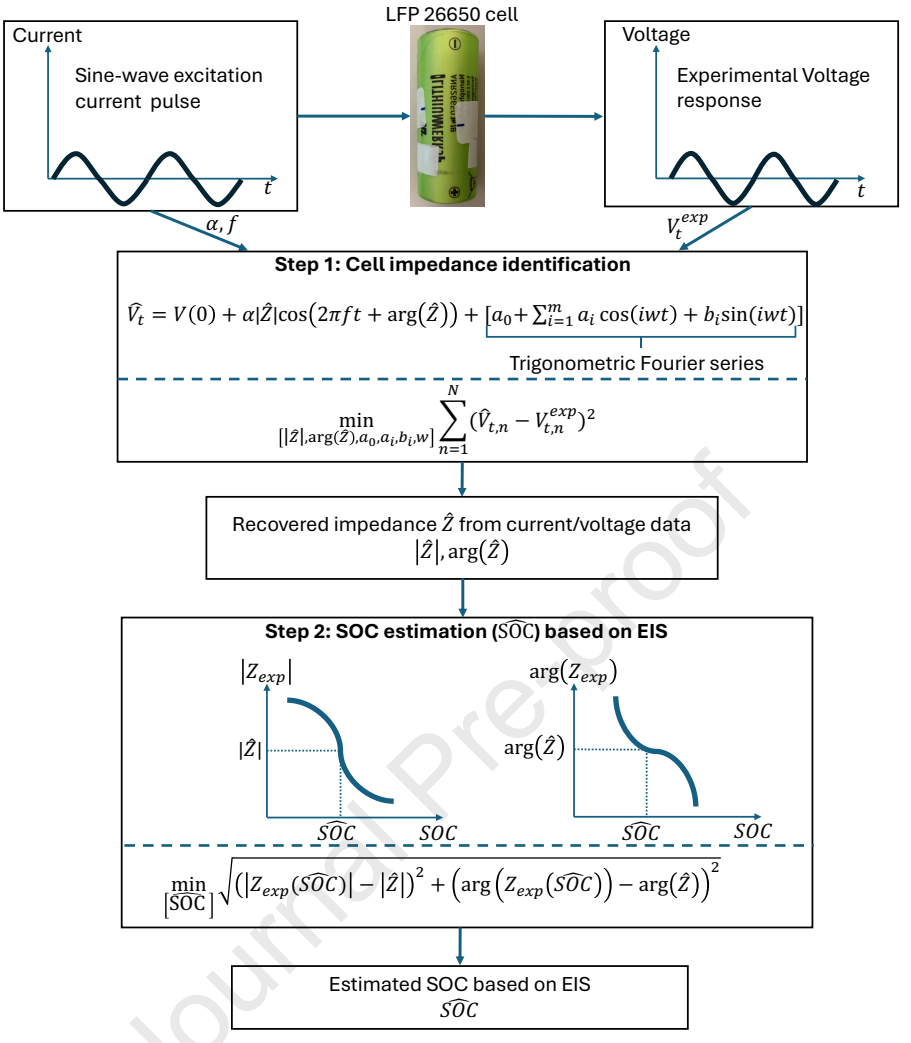

Figure 7: Cell SOC estimation algorithm based on recovered EIS signal with sine-wave current excitation and voltage responses. This algorithm comprises two main components. The first part is the EIS identification and recovery process of sine-wave current pulse excitation. The second part is the SOC estimation based on the recovered EIS signal.

where $V_t(0)$ is the cell OCV. Generally, the actual battery voltage includes a transient term $V_{transient}$, which diminishes over time [39]. So, the realistic voltage response can be represented by the following format:

$$\hat{V}_t = V_t(0) + \alpha |Z| \cos(2\pi f t + \arg(Z)) + V_{transient} \tag{6}$$

We choose to use the Trigonometric Fourier series to approximate the $V_{transient}$. Consequently, $\hat{V}_t$ becomes:

$$\hat{V}_t = V_t(0) + \alpha |Z| \cos(2\pi f t + \arg(Z)) + \underbrace{\left[a_0 + \sum_{i=1}^{m} \left(a_i \cos(i\omega t) + b_i \sin(i\omega t)\right)\right]}_{\text{Trigonometric Fourier Series}} \tag{7}$$

where a_0 is the constant term in the transient voltage, w is the fundamental frequency of the transient voltage, and m is the number of terms. The order m of the trigonometric Fourier series is determined empirically to balance accuracy and robustness. We performed cross-validation by gradually increasing m and evaluating the resulting RMSE between fitted and experimental voltage responses. It was observed that adding more than 5–7 harmonics produced only marginal improvements in RMSE, while unnecessarily increasing model complexity and risk of overfitting. Therefore, m was limited within this range to ensure reliable impedance recovery while avoiding underfitting at low orders and preserving computational efficiency suitable for online BMS applications.

To estimate the parameters including the $|Z|$, $\arg(Z)$, a_0, a_i, b_i, and w, the following objective function is formulated:

$$\min_{[|\hat{Z}|,\arg(\hat{Z}),a_0,a_i,b_i,w]} \sum_{n=1}^{N} (\hat{V}_{t,n} - V_{t,n}^{exp})^2 \tag{8}$$

where $\hat{V}_{t,n}$ is the n-th data point of the fitted voltage vector in Eq.7. $V_{t,n}^{exp}$ is the n-th data point of the experimental measured voltage. N is the length of the experimental voltage data. The Curve Fitting Toolbox in Matlab is used to perform this parameter estimation calculation. Therefore, given the experimental voltage responses to the sine-wave current pulses ($V_{t,n}^{exp}$), these parameters including the cell impedance are optimized by fitting the experimental data with Eq.8.

Traditional EIS measurements are generally performed under strict steady-state conditions, which often necessitate long resting periods to eliminate transient relaxation effects. Such requirements limit the feasibility of EIS integration into online BMS applications. In contrast, the proposed framework mitigates this constraint by employing short-duration sinusoidal current pulses combined with Fourier series expansion of the transient voltage response. This strategy effectively reconstructs the impedance spectrum without requiring full equilibrium, thereby reducing measurement time and rest dependence. As a result, the method provides a more practical pathway for extracting SOC-sensitive impedance features in real-time battery operation.

Based on the recovered impedance from current/voltage data ($|\hat{Z}|, \arg(\hat{Z})$), the EIS-based SOC estimation algorithm is developed. It is assumed that the experimental EIS Z_{exp} vs. SOC is stored as the benchmark values. Once the recovered EIS, $\hat{Z}$ is obtained, the estimated SOC, $\widehat{SOC}$ can be solved as a two-dimensional lookup table problem as follows:

$$\min_{\left[\widehat{\mathrm{SOC}}\right]} \sqrt{\left(\left|Z_{exp}(\widehat{SOC})\right| - \left|\hat{Z}\right|\right)^2 + \left(arg\left(Z_{exp}\left(\widehat{SOC}\right)\right) - arg(\hat{Z})\right)^2} \tag{9}$$

where $\widehat{SOC}$ is the estimated SOC that minimizes the difference between the recovered EIS ($(|\hat{Z}|, \arg(\hat{Z}))$ and the experimental EIS ($|Z_{exp}|, arg(Z_{exp})$). The *min* function in Matlab is utilized to facilitate this process. This procedure represents an open-loop SOC estimation approach, as the SOC is inferred directly from the recovered cell impedance without any feedback correction, in contrast to closed-loop estimation strategies.

4. Experimental results

In this section, we validate the EIS recovered algorithm and the EIS-based SOC estimation framework.

4.1. EIS recovery results

The effectiveness of the EIS recovery method, as shown in Fig. 8, is validated using sine-wave current testing data, where the cell impedance is reconstructed by fitting the measured current–voltage response at each excitation frequency. Fig. 8a compares the experimental voltage responses to sine-wave currents (amplitude: 0.1A, frequency: 0.01Hz) at various SOC values during discharge, alongside the fitted voltage curves. The fitted curves (in red) closely align with the actual voltage profiles (in blue) across the SOC

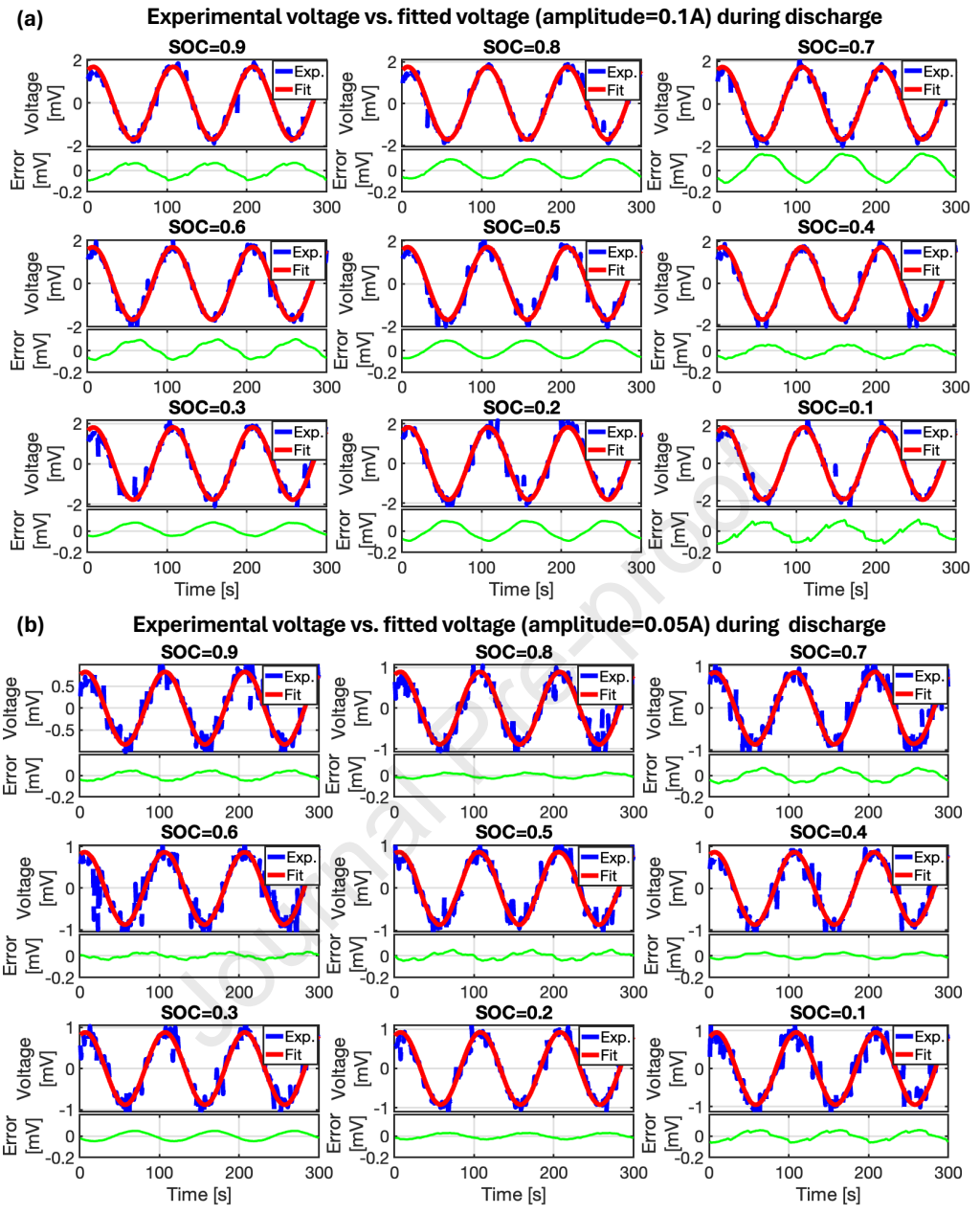

Figure 8: Impedance identification process: (a) Comparison between experimental voltage responses (blue line) to sine-wave current (amplitude=0.1A) and fitted voltage (red line) under different SOC points during discharge and the fitting error (green line).(b) Comparison between experimental voltage responses (blue line) to sine-wave current (amplitude=0.05A) and fitted voltage (red line) under different SOC points during discharge and the fitting error (green line).

values, demonstrating a strong agreement between the model and experimental data. The RMSE values of the voltage fitting during impedance identification, listed in Table 2, are all below 0.232 mV. In Fig. 8b, when the current amplitude is set to 0.05 A, the experimental voltage profiles show increased noise due to a lower SNR. However, the fitted voltage curves still match the experimental data well across all SOC values, with RMSEs under 0.22 mV. The impedance identification results during charge are provided in the Appendix for brevity. As Table 2 shows, the EIS identification method consistently fits voltage with RMSE values below 0.22 mV during charge.

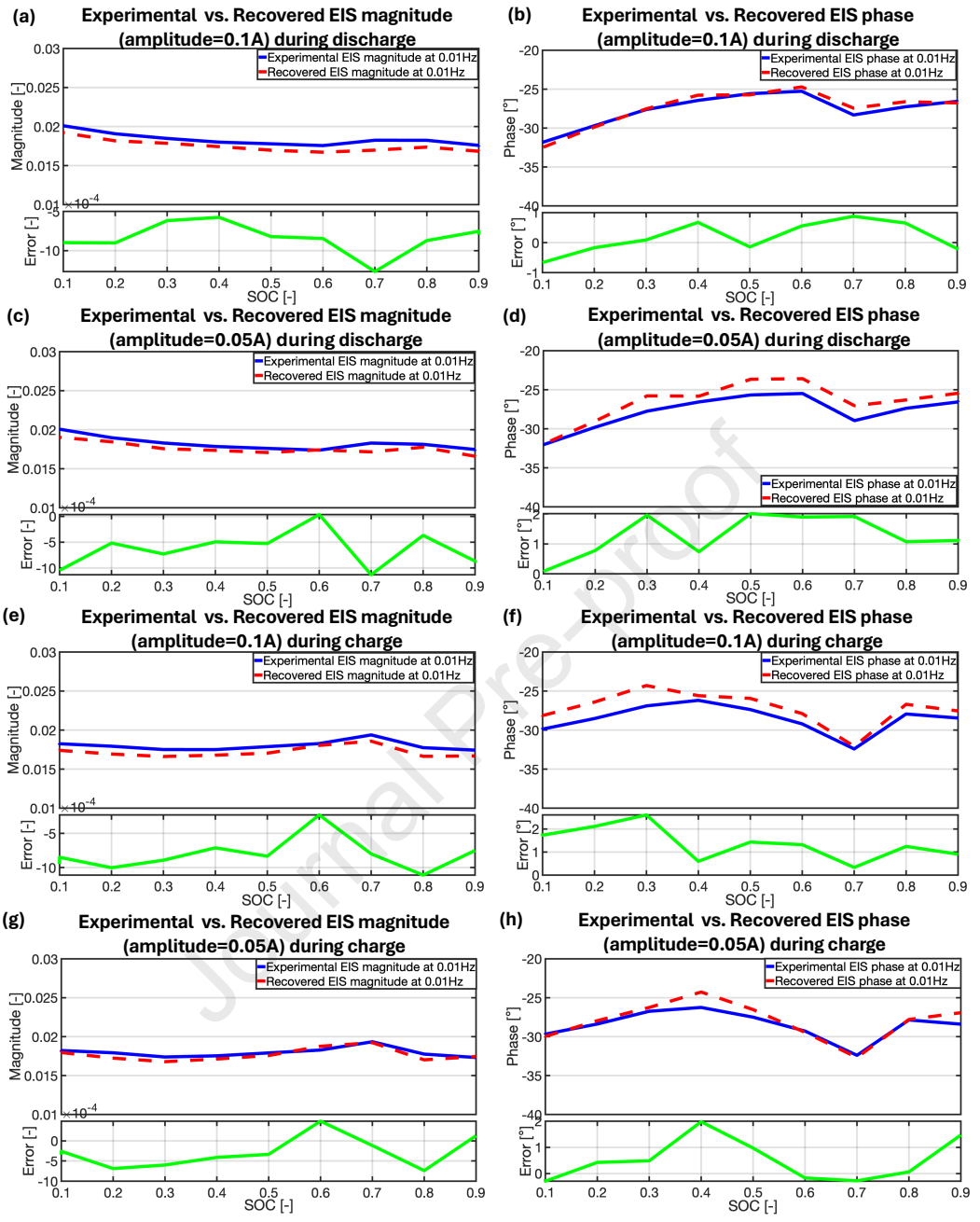

Figure 9: Experimental EIS magnitude (a) and phase (b) versus the recovered results obtained using a 0.1 A excitation during discharge, together with the corresponding fitting errors; Experimental and recovered EIS magnitude (c) and phase (d) under a 0.05 A excitation during discharge, with the associated fitting errors; Experimental and recovered EIS magnitude (e) and phase (f) obtained using a 0.1 A excitation during charge, with the fitting errors; Experimental and recovered EIS magnitude (g) and phase (h) under a 0.05 A excitation during charge, together with the fitting errors.

The comparison between the identified EIS magnitude and phase at 0.01 Hz and the experimental EIS data is illustrated in Fig. 9, with the RMSEs summarized in Table 3. In Fig. 9a, the recovered EIS magnitude at discharge, with an amplitude of 0.1A, closely matches the experimental EIS magnitude. The RMSE of the EIS magnitude recovery is 8.60×10^{-4}. Similarly, Fig. 9b demonstrates that the identified EIS phase

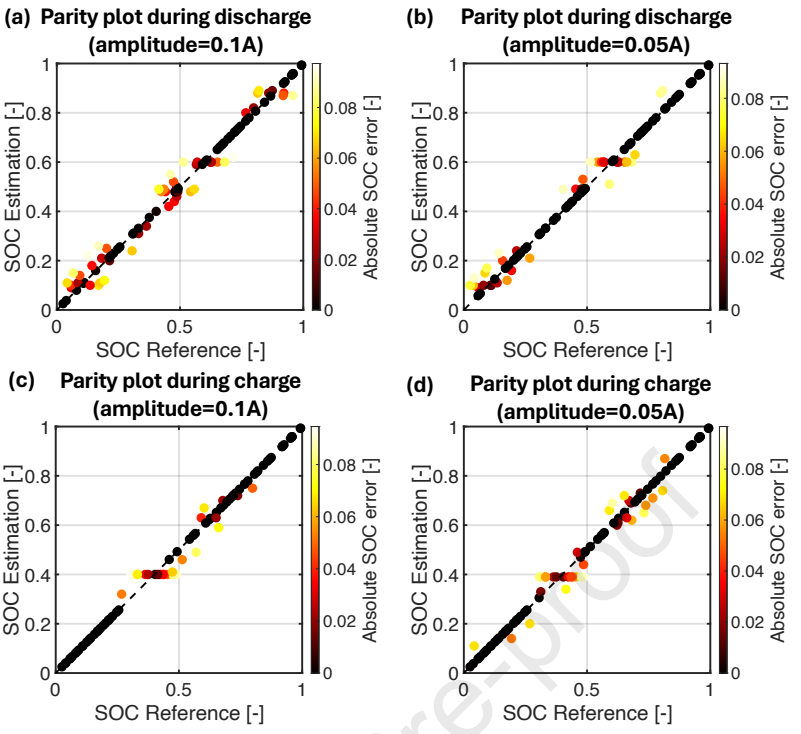

Figure 10: EIS-based SOC estimation results. (a) Parity plot of EIS-based SOC estimation (amplitude=0.1A) during discharge.(b) Parity plot of EIS-based SOC estimation (amplitude=0.05A) during discharge.(c) Parity plot of EIS-based SOC estimation (amplitude=0.1A) during charge.(d) Parity plot of EIS-based SOC estimation (amplitude=0.05A) during charge.

Table 2
RMSEs of voltage recovery during the impedance identification process [mV]

SOC	0.9	0.8	0.7	0.6	0.5	0.4	0.3	0.2	0.1
Amplitude=0.1A, discharge [mV]	0.164	0.167	0.173	0.193	0.232	0.173	0.225	0.223	0.202
Amplitude=0.05A, discharge [mV]	0.168	0.191	0.179	0.218	0.156	0.144	0.148	0.128	0.203
Amplitude=0.1A, charge [mV]	0.209	0.173	0.183	0.203	0.156	0.162	0.183	0.212	0.188
Amplitude=0.05A, charge [mV]	0.203	0.186	0.208	0.215	0.177	0.140	0.185	0.198	0.219

at discharge direction, with an amplitude of 0.1A, aligns well with the experimental results, yielding an RMSE of 0.528°.

As the current amplitude decreases to 0.05A, Fig. 9c illustrates that the recovered magnitude at 0.01Hz maintains accurate recovery of the experimental magnitude, with an RMSE of 7.13×10^{-4}. In Fig. 9d, the RMSE of the EIS phase recovery is 1.44°. For charge directions, Fig. 9e-h depicts that the estimated EIS magnitudes and phases effectively track the experimental EIS results. The RMSEs of the EIS magnitude and phase recoveries, with an amplitude of 0.1A in the charge direction, are 8.31×10^{-4} and 1.523°, respectively. Additionally, the RMSEs of the EIS magnitude and phase recoveries, with an amplitude of 0.05A in the charge direction, are 4.72×10^{-4} and 0.919°, respectively. These results indicate that the proposed EIS recovery method accurately identifies the EIS magnitude and phase based on sine-wave current and voltage data.

4.2. EIS-based SOC estimation results

Here, we evaluate the efficacy of the EIS-based SOC estimation method, utilizing experimental EIS as the reference. We introduce a random initial SOC error to assess the effectiveness of the estimator. The initial SOC errors, with RMSE, mean absolute value, minimum, and maximum values of 0.0571, 0.0495, -0.0974, and 0.0968, respectively, are added deliberately. SOC estimation is achieved by minimizing the discrepancy

Table 3
RMSEs of recovered EIS magnitude and phase

	EIS magnitude [-]	EIS phase [°]
Amplitude=0.1A, in discharge	8.60×10^{-4}	0.528
Amplitude=0.05A, in discharge	7.13×10^{-4}	1.440
Amplitude=0.1A, in charge	8.31×10^{-4}	1.523
Amplitude=0.05A, in charge	4.72×10^{-4}	0.919

Table 4
RMSEs, mean absolute, minimum, maximum, number of SOC estimations when estimation error<initial SOC error (N_1), number of SOC estimations when estimation error=initial SOC error (N_2), and number of SOC estimations when estimation error>initial SOC error (N_3).

	RMSE	Mean absolute	Minimum	Maximum	N_1	N_2	N_3
Initial SOC	0.0571	0.0495	-0.0974	0.0968			
EIS-based SOC estimation error when Amplitude=0.1A, discharge direction	0.0470	0.0366	-0.0974	0.09	55	23	23
EIS-based SOC estimation error when Amplitude=0.05A, discharge direction	0.0662	0.0540	-0.15	0.14	31	30	40
EIS-based SOC estimation error when Amplitude=0.1A, charge direction	0.0614	0.0512	-0.11	0.16	31	33	37
EIS-based SOC estimation error when Amplitude=0.05A, charge direction	0.0534	0.0418	-0.16	0.0918	42	29	30

between recovered and experimental EIS over a range from 0 to 1, with 101 SOC points explored at 0.01 intervals. These points are categorized into N_1, N_2, and N_3, denoting SOC estimations with errors less than, equal to, and greater than the initial SOC error, respectively ($N_1 + N_2 + N_3 = 101$).

Fig. 10 summarizes EIS-based SOC estimation results with added initial SOC error. The RMSE, mean absolute value, minimum, and maximum SOC estimation errors are consolidated in Table 4. In Fig. 10a, for a sinusoidal current amplitude of 0.1A in the discharge direction, SOC estimation yields an RMSE of 0.0470 and a mean absolute error of 0.0366. Here, N_1, N_2, and N_3 are 55, 23, and 23, respectively. This suggests that with a 0.1A discharge, the EIS-based SOC estimation accurately resets initial SOC values at 55 SOC points across the entire range. Moreover, the RMSE and mean absolute error of SOC estimations are lower than initial SOC errors, indicating the effectiveness of the EIS-based method in error reduction. With a decrease in current amplitude to 0.05A in the discharge direction, SOC estimation results (Fig. 10b) show N_1, N_2, and N_3 as 31, 30, and 40, respectively. While the EIS-based method still mitigates initial SOC errors at 31 points, the number decreases compared to 0.1A amplitude. Additionally, the RMSE and mean absolute value of SOC estimation errors increase, as shown in Table 4, due to the larger RMSE of the recovered EIS phase at 0.05A amplitude. The performance degradation observed at a current amplitude of 0.05 A can be attributed primarily to the reduced SNR. Lower excitation currents produce weaker voltage responses, which become more susceptible to measurement noise and result in less accurate recovery of the EIS phase. Since SOC estimation in our framework relies strongly on precise phase identification, this noise sensitivity leads to degraded accuracy. Additionally, small nonlinearities in the electrode processes may further contribute to the discrepancy under very low excitation amplitudes. Similar trends are observed for charge direction at 0.1A amplitude (Fig. 10c), where a larger RMSE and mean absolute value of EIS-based SOC estimation errors are noted compared to initial SOC errors. However, only 31 SOC points contribute to error reduction. Conversely, at 0.05A amplitude in charge direction (Fig. 10d), superior performance is observed with lower RMSE and mean absolute value of EIS-based SOC estimation errors (0.0534 and 0.0418, respectively), and an increase in N_1 to 42. These results underscore the dependency of EIS-based SOC estimation effectiveness on the accuracy of the recovered EIS signal, with the 0.1A discharge scenario exhibiting optimal performance among the investigated cases.

4.3. Discussion

The proposed methodology builds upon the general framework of EIS-based SOC estimation but introduces several distinctive contributions. First, instead of relying on dedicated impedance analyzers, we demonstrate that short-duration sinusoidal current pulses can effectively reconstruct the EIS response directly from current and voltage signals. This approach eliminates the dependency on specialized instrumentation and leverages signals already available in practical BMS environments, thereby enhancing feasibility for large-scale deployment. Second, a systematic SNR-based analysis identifies 0.01 Hz as the frequency with the strongest SOC dependence and the highest robustness to noise. This finding directly addresses the long-standing challenge of the flat OCV–SOC curve in LFP cells and provides a quantitative basis for frequency selection, which has often been heuristic in prior studies. Compared with existing multi-frequency or ECM-fitting methods, our framework achieves a faster and more practical solution for SOC initialization, with direct relevance to on-board applications.

Compared with recent fast EIS methods based on multi-sine or PRBS excitations [32, 40, 41], our framework emphasizes simplicity and direct relevance to SOC. While broadband approaches reconstruct the full spectrum but require sophisticated excitation signals and heavy post-processing, our method uses only a single low-frequency sine perturbation (0.01 Hz) that directly captures the most SOC-sensitive impedance feature. This avoids specialized hardware, reduces computational overhead, and enhances SNR, enabling rapid SOC initialization under practical BMS conditions. Thus, the proposed approach prioritizes simplicity, robustness, and online applicability, offering a distinct advantage over existing fast-EIS strategies.

Several limitations should be acknowledged. The experiments were performed with relatively small excitation amplitudes (0.05 A and 0.1 A) and at a single frequency (0.01 Hz). These conditions were deliberately chosen to highlight the most SOC-sensitive operating point but do not fully represent broader applicability. Another limitation is that OCV hysteresis effects were not considered. Because hysteresis arises from path-dependent electrode processes, neglecting it may cause small discrepancies during charge/discharge transitions. While its impact is modest relative to the improvements of our impedance-based approach, future integration with hysteresis models (e.g., Preisach-type or data-driven corrections) could further improve SOC accuracy. Finally, all experiments were conducted under controlled isothermal conditions. Given that impedance spectra are strongly temperature-dependent, variations in ambient or cell temperature could alter the SOC–EIS relationship. We also acknowledge that the current amplitude range examined here is relatively narrow.

Despite these restrictions, this study demonstrates a rapid and cost-effective strategy for SOC initialization, distinct from methods targeting full-spectrum impedance reconstruction. By showing that robust SOC features can be recovered from simple short-pulse excitations, we highlight a practical pathway to integrate EIS-based estimation into BMS without imposing significant hardware or time overhead.

5. Conclusion

This paper proposes a rapid EIS-based SOC estimation method utilizing short-duration sine-wave current profiles. Experimental EIS data of LFP batteries, obtained with current amplitudes of 0.05 A and 0.1 A across various frequencies and SOC ranges, are analyzed. Among these, the cell EIS measured at 0.01 Hz exhibits the highest SNR, making it suitable as a benchmark for EIS-based SOC estimation. To efficiently recover the cell EIS at 0.01 Hz within a short timeframe, sine-wave current profiles are applied to the cell, and the voltage responses are approximated using the Fourier series. Subsequently, the magnitude and phase of the cell EIS are accurately derived by fitting the approximated voltage to the experimental voltage data. Based on the recovered EIS signal, the cell SOC is estimated by correlating the recovered EIS signal with experimental SOC-dependent EIS data. Finally, this SOC estimation approach is validated using sine-wave currents with amplitudes of 0.05 A and 0.1 A in both the discharge and charge directions. Experimental findings verify the effectiveness of the EIS-based SOC estimation strategy.

Future work will expand the range of excitation currents and frequencies, and benchmark the method against state-of-the-art rapid EIS acquisition techniques. Furthermore, integration with OCV hysteresis models (e.g., Preisach-type or data-driven corrections) could further enhance SOC estimation accuracy. Finally, extending the framework to incorporate temperature compensation and systematic validation across

multiple temperatures and current amplitudes will be essential to ensure robustness for real-world BMS applications.

Data availability

The experimental dataset supporting this study is publicly available at: https://github.com/yizhaogao2025/LFP_battery_SOC_Dataset.

Supplementary information

The supplementary information provides additional details on the experimental data used in this study, including the data collection procedures and the structure of the dataset.

Appendix

1) The SNRs of the SOC estimation with EIS magnitude $\left|\hat{Z}\right|$-SOC (SNR_1=$SNR_{\widehat{SOC}_{\left|\hat{Z}\right|-SOC:look-up-table}}$), EIS phase $arg\hat{Z}$-SOC (SNR_2=$SNR_{\widehat{SOC}_{arg\hat{Z}-SOC:look-up-table}}$), and EIS (magnitude & phase)-SOC lookup table(SNR_3=$SNR_{\widehat{SOC}_{\left|\hat{Z}\right|\&arg\hat{Z}-SOC:look-up-table}}$) are calculated with the following equations:

$$\widehat{SOC}_{\left|\hat{Z}\right|-SOC:look-up-table} = f_{\left|\hat{Z}\right|-SOC}\left(\left|\hat{Z}\right|\right) \tag{10}$$

$$\mathrm{SNR}_1 = \mathrm{SNR}_{\widehat{\mathrm{SOC}}_{|\hat{Z}|\text{-SOC:look-up-table}}} = 20\log_{10}\left(\frac{\sqrt{\sum_{n=1}^{N}\left|\widehat{\mathrm{SOC}}_{|\hat{Z}|\text{-SOC:look-up-table},n}\right|^2}}{\sqrt{\sum_{n=1}^{N}|\mathrm{noise}_n|^2}}\right) \tag{11}$$

$$\widehat{SOC}_{arg\hat{Z}-SOC:look-up-table} = f_{arg\hat{Z}-SOC}\left(\left|\hat{Z}\right|\right) \tag{12}$$

$$\mathrm{SNR}_2 = \mathrm{SNR}_{\widehat{\mathrm{SOC}}_{arg\hat{Z}\text{-SOC:look-up-table}}} = 20\log_{10}\left(\frac{\sqrt{\sum_{n=1}^{N}\left|\widehat{\mathrm{SOC}}_{arg\hat{Z}\text{-SOC:look-up-table},n}\right|^2}}{\sqrt{\sum_{n=1}^{N}|\mathrm{noise}_n|^2}}\right) \tag{13}$$

$$\widehat{SOC}_{\left|\hat{Z}\right|\&arg\hat{Z}-SOC:look-up-table} = f_{\left|\hat{Z}\right|\&arg\hat{Z}-SOC}\left(\left|\hat{Z}\right|, arg\hat{Z}\right) \tag{14}$$

$$\mathrm{SNR}_3 = \mathrm{SNR}_{\widehat{\mathrm{SOC}}_{|\hat{Z}|\&\,\arg(\hat{Z})\text{-SOC:look-up-table}}} = 20\log_{10}\left(\frac{\sqrt{\sum_{n=1}^{N}\left|\widehat{\mathrm{SOC}}_{|\hat{Z}|\&\,\arg(\hat{Z})\text{-SOC:look-up-table},n}\right|^2}}{\sqrt{\sum_{n=1}^{N}|\mathrm{noise}_n|^2}}\right) \tag{15}$$

where $f_{|Z|-\mathrm{SOC}}\left(|\hat{Z}|\right)$ is the lookup table function that maps a given EIS magnitude value $|\hat{Z}|$ to the corresponding SOC. Similarly, $f_{\arg\hat{Z}-\mathrm{SOC}}\left(\arg\hat{Z}\right)$ is the lookup table function that maps a given EIS phase value $\arg\hat{Z}$ to the corresponding SOC. Finally, $f_{|Z|\&\arg\hat{Z}-\mathrm{SOC}}\left(|\hat{Z}|, \arg\hat{Z}\right)$ is the lookup table function that maps a given pair of EIS magnitude $|\hat{Z}|$ and EIS phase $\arg\hat{Z}$ values to the corresponding SOC.

2) The Impedance identification processes with sine-wave current (amplitude=0.1A/0.05A) during charge are listed in Fig. 11.

Acknowledgement

The authors would like to thank Stanford Energy Control Lab member Andrea Lanubile for providing helpful comments.

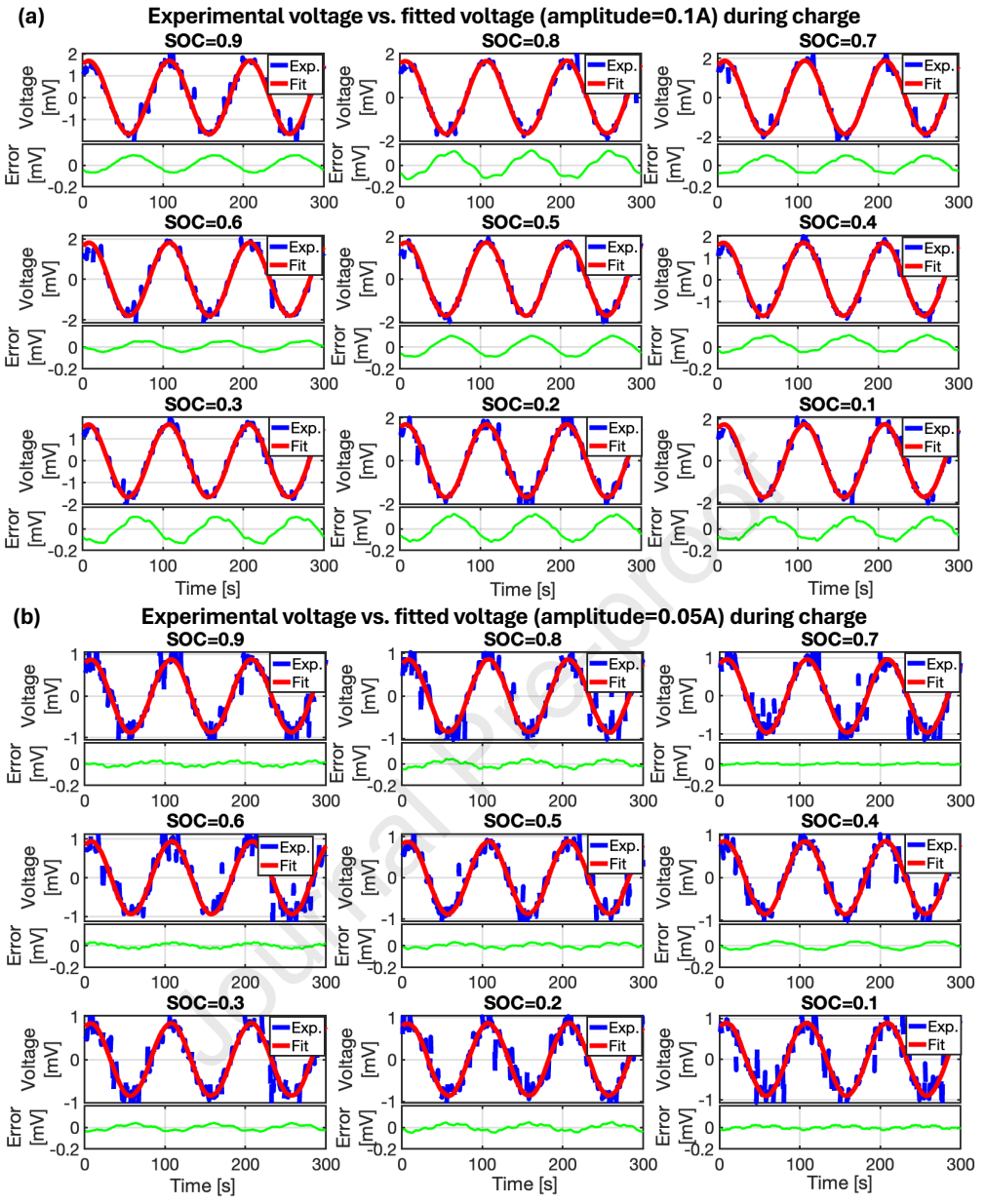

Figure 11: Impedance identification process. (a) Comparison between experimental voltage responses (blue line) to sine-wave current (amplitude=0.1A) and fitted voltage (red line) under different SOC points during charge direction and the fitting error (green line). (b) Comparison between experimental voltage responses (blue line) to sine-wave current (amplitude=0.05A) and fitted voltage (red line) under different SOC points during charge direction and the fitting error (green line).

References

[1] Jan Schöberl, Manuel Ank, Markus Schreiber, Nikolaos Wassiliadis, and Markus Lienkamp. Thermal runaway propagation in automotive lithium-ion batteries with nmc-811 and lfp cathodes: Safety requirements and impact on system integration. *Etransportation*, 19:100305, 2024.

[2] Akshaya K Padhi, Kirakodu S Nanjundaswamy, and John B Goodenough. Phospho-olivines as positive-electrode materials for rechargeable lithium batteries. *Journal of the electrochemical society*, 144(4):1188, 1997.

[3] Gregory L. Plett. Extended kalman filtering for battery management systems of lipb-based hev battery packs: Part 1. background. *Journal of Power Sources*, 134(2):252–261, 2004.

[4] Gregory L. Plett. Sigma-point kalman filtering for battery management systems of lipb-based hev battery packs: Part 1: Introduction and state estimation. *Journal of Power Sources*, 161(2):1356–1368, 2006.

[5] Maoshu Xu, E Zhang, Sheng Wang, Yi Shen, Binchen Zou, Haomiao Li, Yimin Wan, Kangli Wang, and Kai Jiang. Dynamic ultrasonic response modeling and accurate state of charge estimation for lithium ion batteries under various load profiles and temperatures. *Applied Energy*, 355:122210, 2024.

[6] J. A. Braun, R. Behmann, D. Chabrol, F. Fuchs, and W. G. Bessler. Single-cell operando soc and soh diagnosis in a 24 v lithium iron phosphate battery with a voltage-controlled model. *Journal of Energy Storage*, 85:110986, 2024.

[7] Yizhao Gao and Simona Onori. Systems and methods for state-of-charge estimation based on dq/dv curve, June 2025. https://patentscope.wipo.int/search/en/WO2025122659.

[8] Yizhao Gao and Simona Onori. Advancing soc estimation in lifepo4 batteries: Enhanced dq/dv curve and short-pulse methods. *eTransportation*, page 100466, 2025.

[9] M. Sandrabyna and A. Patil. State-of-charge estimation for lifepo4 batteries with adaptive state update in specific ocv ranges using adaptive extended kalman filter. *SAE Technical Paper*, 2024.

[10] B. Yao et al. State-of-charge estimation for lithium-ion batteries based on modified unscented kalman filter using improved parameter identification. *International Journal of Electrochemical Science*, page 100574, 2024.

[11] M. Saeed, S. Lu, Z. Song, and X. Hu. Integrated framework for accurate state estimation of lithium-ion batteries subject to measurement uncertainties. *IEEE Transactions on Power Electronics*, 2024.

[12] Meng Wei, Min Ye, Chuawei Zhang, Gaoqi Lian, Baozhou Xia, and Qiao Wang. Robust state of charge estimation of lifepo4 batteries based on sage_husa adaptive kalman filter and dynamic neural network. *Electrochimica Acta*, 477:143778, 2024.

[13] L. Wang et al. A novel ocv curve reconstruction and update method of lithium-ion batteries at different temperatures based on cloud data. *Energy*, 268:126773, 2023.

[14] Yizhao Gao and Simona Onori. Systems and methods for state-of-charge estimation using sine-wave current pulses, June 2025. https://patents.google.com/patent/WO2025122661A1.

[15] Y. Ko and W. Choi. A new soc estimation for lfp batteries: Application in a 10 ah cell (hw 38120 l/s) as a hysteresis case study. *Electronics*, 10(6), 2021.

[16] Y. Li et al. Early warning method for thermal runaway of lithium-ion batteries under thermal abuse condition based on online electrochemical impedance monitoring. *Journal of Energy Chemistry*, 92:74–86, 2024.

[17] A. La Rue, P. J. Weddle, M. Ma, C. Hendricks, R. J. Kee, and T. L. Vincent. State-of-charge estimation of lifepo4–li4ti5o12 batteries using history-dependent complex-impedance. *Journal of The Electrochemical Society*, 166(16):A4041, 2019.

[18] U. Westerhoff, T. Kroker, K. Kurbach, and M. Kurrat. Electrochemical impedance spectroscopy based estimation of the state of charge of lithium-ion batteries. *Journal of Energy Storage*, 8:244–256, 2016.

[19] B. G. Carkhuff, P. A. Demirev, and R. Srinivasan. Impedance-based battery management system for safety monitoring of lithium-ion batteries. *IEEE Transactions on Industrial Electronics*, 65(8):6497–6504, 2018.

[20] J.-H. Lee and W.-J. Choi. Novel state-of-charge estimation method for lithium polymer batteries using electrochemical impedance spectroscopy. *Journal of Power Electronics*, 11(2):237–243, 2011.

[21] J. Xu, C. C. Mi, B. Cao, and J. Cao. A new method to estimate the state of charge of lithium-ion batteries based on the battery impedance model. *Journal of Power Sources*, 233:277–284, 2013.

[22] N. Chen, P. Zhang, J. Dai, and W. Gui. Estimating the state-of-charge of lithium-ion battery using an h-infinity observer based on electrochemical impedance model. *IEEE Access*, 8:26872–26884, 2020.

[23] R. Mingant et al. Eis measurements for determining the soc and soh of li-ion batteries. *ECS Transactions*, 33(39):41, 2011.

[24] Colin J Chu, Sai Thatipamula, and Simona Onori. Frequency-based parameterization of semi-empirical models for state-of-health estimation in lithium-ion batteries. *Journal of The Electrochemical Society*, 172(10):100540, 2025.

[25] E. Buchicchio, A. De Angelis, F. Santoni, P. Carbone, F. Bianconi, and F. Smeraldi. Battery soc estimation from eis data based on machine learning and equivalent circuit model. *Energy*, 283:128461, 2023.

[26] M. Messing, T. Shoa, R. Ahmed, and S. Habibi. Battery soc estimation from eis using neural nets. In *2020 IEEE Transportation Electrification Conference Expo (ITEC)*, pages 588–593. IEEE, 2020.

[27] Xi Anjing. *Experimental study on Electrochemical impedance spectroscopy of lithium iron phosphate batteries*. PhD thesis, Tsinghua University, Beijing, 2012.

[28] A. De Angelis, P. Z. Csurcsia, V. Brunacci, and P. Carbone. Fast battery eis measurement using flexible local rational method. *IEEE Transactions on Instrumentation and Measurement*, 73:1–10, 2024.

[29] X. Wang, X. Wei, Q. Chen, J. Zhu, and H. Dai. Lithium-ion battery temperature on-line estimation based on fast impedance calculation. *Journal of Energy Storage*, 26:100952, 2019.

[30] C. Lyu, H. Liu, W. Luo, T. Zhang, and W. Zhao. A fast time domain measuring technique of electrochemical impedance spectroscopy based on fft. In *2018 Prognostics and System Health Management Conference (PHM-Chongqing)*, pages 450–455. IEEE, 2018.

[31] Y. Fu, J. Xu, M. Shi, and X. Mei. A fast impedance calculation-based battery state-of-health estimation method. *IEEE Transactions on Industrial Electronics*, 69(7):7019–7028, 2021.

[32] J. Sihvo, D.-I. Stroe, T. Messo, and T. Roinila. Fast approach for battery impedance identification using pseudo-random sequence signals. *IEEE Transactions on Power Electronics*, 35(3):2548–2557, 2019.

[33] X. Liu et al. Binary multi-frequency signal for accurate and rapid electrochemical impedance spectroscopy acquisition in lithium-ion batteries. *Applied Energy*, 364:123221, 2024.

[34] A. La Rue. *Small-signal wide-band electrochemical-impedance measurements for battery management*. PhD thesis, 2019.

[35] K. Mc Carthy, H. Gullapalli, K. M. Ryan, and T. Kennedy. Review—use of impedance spectroscopy for the estimation of li-ion battery state of charge, state of health and internal temperature. *Journal of The Electrochemical Society*, 168(8), 2021.

[36] D. A. Howey, P. D. Mitcheson, V. Yufit, G. J. Offer, and N. P. Brandon. Online measurement of battery impedance using motor controller excitation. *IEEE Transactions on Vehicular Technology*, 63(6):2557–2566, 2013.

[37] J. Kim and J. Kowal. A method for monitoring state-of-charge of lithium-ion cells using multi-sine signal excitation. *Batteries*, 7(4):76, 2021.

[38] Edoardo Catenaro and Simona Onori. Experimental data of lithium-ion batteries under galvanostatic discharge tests at different rates and temperatures of operation. *Data in Brief*, 35:106894, 2021.

[39] Xiangdong Kong, Gregory L Plett, M Scott Trimboli, Zhendong Zhang, and Yuejiu Zheng. An exact closed-form impedance model for porous-electrode lithium-ion cells. *Journal of The Electrochemical Society*, 167(1):013539, 2020.

[40] Lujun Wang, Ziang Song, Lijun Zhu, and Jiuchun Jiang. Fast electrochemical impedance spectroscopy of lithium-ion batteries based on the large square wave excitation signal. *IScience*, 26(4), 2023.

[41] Ling Zhu, Jichang Peng, Jinhao Meng, Chenghao Sun, Lei Cai, and Zhizhu Qu. Fast impedance spectrum construction for lithium-ion batteries using a multi-density clustering algorithm. *Batteries*, 10(3):112, 2024.

Rapid EIS-based SOC estimation method for LiFePO4 batteries using sine-wave currents.

EIS at 0.01 Hz shows highest signal-to-noise ratio for accurate SOC estimation.

SOC estimation algorithm addresses challenges posed by flat OCV-SOC curve in LFP cells.

Sine-wave pulses effectively reconstruct EIS, achieving reliable SOC prediction.

Practical SOC estimation without costly equipment using current/voltage signal data.

Declaration of interests

☒ The authors declare that they have no known competing financial interests or personal relationships that could have appeared to influence the work reported in this paper.

☐ The authors declare the following financial interests/personal relationships which may be considered as potential competing interests:

Advancing $LiFePO_4$ Battery SOC Estimation: Electrochemical Impedance Spectroscopy with Short-Period Sine-Wave Pulses

Yizhao Gao*, Simona Onori*

Department of Energy Science and Engineering, Stanford University, Stanford, CA 94305, USA

*Corresponding author, yizhaog@stanford.edu, sonori@stanford.edu;

Author contribution:

Yizhao Gao: Conceptualization, Methodology, Software, Data Curation, Validation, Writing - Original Draft.

Simona Onori: Visualization, Writing - Review & Editing.

Acknowledgement:

The authors would like to thank Stanford Energy Control Lab member Andrea Lanubile for providing helpful comments.